Arefeh Abbasi
Ecole Polytechnique Fédérale de Lausanne (EPFL),
Flexible Structures Laboratory,
CH-1015 Lausanne, Switzerland
e-mail: arefeh.abbasi@epfl.ch

Fani Derveni
Ecole Polytechnique Fédérale de Lausanne (EPFL),
Flexible Structures Laboratory,
CH-1015 Lausanne, Switzerland
e-mail: fani.derveni@epfl.ch

Pedro M. Reis[1]
Ecole Polytechnique Fédérale de Lausanne (EPFL),
Flexible Structures Laboratory,
CH-1015 Lausanne, Switzerland
e-mail: pedro.reis@epfl.ch

Comparing the Buckling Strength of Spherical Shells With Dimpled Versus Bumpy Defects

We investigate the effect of defect geometry in dictating the sensitivity of the critical buckling conditions of spherical shells under external pressure loading. Specifically, we perform a comparative study between shells containing dimpled (inward) versus bumpy (outward) Gaussian defects. The former has become the standard shape in many recent shell-buckling studies, whereas the latter has remained mostly unexplored. We employ finite-element simulations, which were validated previously against experiments, to compute the knockdown factors for the two cases while systematically exploring the parameter space of the defect geometry. For the same magnitudes of the amplitude and angular width of the defect, we find that shells containing bumpy defects consistently exhibit significantly higher knockdown factors than shells with the more classic dimpled defects. Furthermore, the relationship of the knockdown as a function of the amplitude and the width of the defect is qualitatively different between the two cases, which also exhibit distinct post-buckling behavior. A speculative interpretation of the results is provided based on the qualitative differences in the mean-curvature profiles of the two cases. [DOI: 10.1115/1.4056801]

Keywords: elasticity, stress analysis, structures

1 Introduction

The mechanical response of thin elastic shells under compression is highly nonlinear [1,2], with a strong sensitivity to imperfections [3–6]. Predicting the buckling strength of shells is a long-standing canonical problem in the structural mechanics community [7,8]. The classic prediction for the perfect spherical shell case was first obtained by Zoelly in 1915 [9] from linear buckling analysis:

$$p_c = \frac{2E}{\sqrt{3(1-\nu^2)}}\eta^{-2} \tag{1}$$

where E, ν, and $\eta = R/h$ are the Young's modulus, Poisson's ratio, and slenderness ratio of the shell of radius R and thickness h, respectively. However, experimental measurements for the critical buckling pressure of a thin spherical shell containing imperfections [10–16] are always found to be lower than the theoretical prediction in Eq. (1) due to their extreme sensitivity to imperfections [5]. The discrepancies between theory and experiments have been attributed to the nonuniformity of loading [17], the boundary conditions [18], the influence of pre-buckling deformations [19], and the deviations from perfect shell geometry [20]. The ratio between the measured critical pressure, p_{max}, and the corresponding classic prediction for the perfect geometry, $p_{c,}$ is known as the *knockdown factor*,

$$\kappa = \frac{p_{max}}{p_c} \tag{2}$$

which is always smaller than unity ($\kappa < 1$) for realistic shells that inevitably contain material and geometric imperfections. Despite the classic, albeit still challenging, nature of the problem, there has been a recent revival in the interest and research of shell buckling. The study of the critical buckling conditions of spherical shells has been reinvigorated by recent advances in experiments and computation [16,21–28]. For a contemporary perspective and overview of the recent activity in the field, we point the reader to the following recent studies [16,22–24,29–36]. Even if similar results are also found for cylindrical shells [7,17,20,25,27,37–40], the present study will focus on spherical shells exclusively.

Most of the recent investigations on spherical shell buckling mentioned in the previous paragraphs [33–35,41–43] have considered standardized dimpled (Gaussian) defects. Other types of imperfections (e.g., through-thickness defects [23,44,45], and dent imperfections [46]) have also been considered, but such cases are sparser. A benefit of focusing on standardized dimples is that they allow for a better contextualization and interpretation of results across different studies. These dimpled imperfections are axisymmetric, localized, and characterized by a radial modulation of the shell mid-surface from a perfect sphere of radius R, by

$$w_I = c\delta e^{-(\beta/\beta_\circ)^2} \tag{3}$$

where β is the polar angle measured from the north pole ($\beta = 0$, where the center of the defect is located), and the constants $\beta_\circ$ and δ control the width and amplitude of the defect (see Fig. 1). The defect amplitude, which is typically normalized by the thickness of the shell, $\bar{\delta} = \delta/h$, corresponds to the maximum radial deviation at the center of the defect. It is also common to define a geometric parameter [47],

$$\lambda = \left\{12\left(1-\nu^2\right)\right\}^{1/4}\eta^{1/2}\beta_\circ \tag{4}$$

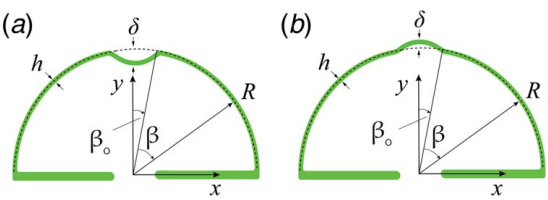

Fig. 1 Schematic diagrams of the two types of geometry considered for our imperfect shells containing (*a*) a dimpled defect and (*b*) a bumpy defect, with $c = -1$ and $c = +1$ (compared with Eq. (3)), respectively. In both cases, the hemispherical shells have radius R and thickness h, and the defect is located at the pole ($\beta = 0$) with a geometry characterized by the amplitude, δ, and half-angular width, $\beta_\circ$.

[1]Corresponding author.

Contributed by the Applied Mechanics Division of ASME for publication in the Journal of Applied Mechanics. Manuscript received December 9, 2022; final manuscript received January 27, 2023; published online March 3, 2023. Assoc. Editor: Pradeep Sharma.

to rescale the defect width, normalizing effects arising from the radius-to-thickness ratio, η, of the shell.

In the existing literature, the prefactor c in Eq. (3) has been consistently set to $c=-1$, corresponding to inward-pointing dimples, as shown schematically in Fig. 1(*a*). The knockdown factor, κ, of such shells containing dimpled defects was found in experiments, as well as theoretical and computational analyses, to depend strongly on $\overline{\delta}$, dropping sharply from unity for $0<\overline{\delta}\lesssim 1$ and reaching a plateau for $\overline{\delta}\gtrsim 1$ [16]. Moreover, these results demonstrated that the geometric parameter λ governs the onset and level of the plateau in the $\kappa(\overline{\delta})$ curves, as characterized thoroughly in Ref. [29]. The authors revealed a lower bound of the plateau level that depends solely on η and λ.

Here, we revisit the buckling of a spherical shell containing a single Gaussian defect according to Eq. (3). We perform a comparative study of the knockdown factor for the previously considered dimpled (inward) defects ($c=-1$; see Fig. 1(*a*)) compared to the symmetric case for bumpy (outward) defects ($c=+1$; see Fig. 1(*b*)). Recently, Derveni et al. [32] have studied the buckling of shells containing a large distribution of defects, validating FEM simulations against experiments using bumpy defects, a choice that was driven by practical experimental constraints, but the difference between dimples and bumps was not explored in detail. Otherwise, to the best of our knowledge, bumpy defects have not been investigated systematically to date. We will focus on the following research question: How does the buckling strength compare between single-imperfection shells containing a dimpled versus a bumpy defect?

2 Methodology: Finite Element Analysis

In Fig. 1, we present schematic diagrams of the two types of geometries for the imperfect hemispherical shells that we will consider, containing either a dimpled defect ($c=-1$ in (*a*)) or a bumpy defect ($c=+1$ in (*b*)). We will focus on hemispherical shells of radius $R=24.85$ mm, thickness $h=0.23$ mm, and thus, $\eta=R/h=108$ with a single imperfection located at the pole, without loss of generality [41] given the large value of η. This generality assumes there is essentially no dependence of knockdown factor characterization on η for sufficiently slender shells as long as the defect width is scaled according to Eq. (4). Each shell is clamped at the equator and (de)pressurized to load it under compression until buckling occurs.

The initial shell geometry considered in the simulations is axisymmetric. As such, the 2D cross-sectional profiles of the imperfect shells presented in Fig. 2 for different values of $\overline{\delta}$ and λ (see color bar) suffice to fully describe this initial geometry. The perfectly spherical case ($\overline{\delta}=0$, $\lambda=0$) is represented by the dashed line. (*a*, *c*) and (*b*, *d*) represent the shell with dimpled ($c=-1$) and bumpy ($c=+1$) defects, respectively. Representative defects with the same defect width, $\lambda=2.5$, in a range of amplitudes, $\overline{\delta}\in\{1, 2, 3, 4, 5\}$, are shown in Figs. 2(*a*) and 2(*b*). In Figs. 2(*c*) and 2(*d*), we present representative shell profiles with the same defect amplitude, $\overline{\delta}=2.5$, in a range of widths, $\lambda\in\{1, 2, 3, 4, 5\}$. The corresponding lower panels in Fig. 2 show magnified views of the defect profiles localized at the pole. Beyond these representative cases, our investigation will consider the following ranges for the geometric parameters space of the defect: $\overline{\delta}\in[0.1,\ 5]$ in steps of $\Delta\overline{\delta}=0.1$ for the defect amplitude and $\lambda\in[0.25,\ 5]$ in steps of $\Delta\lambda=0.25$ for $\lambda\le 1$ and $\Delta\lambda=0.5$ for $\lambda\ge 1$ for the (normalized) defect width, while fixing all other parameters mentioned earlier. Although these initial geometries are axisymmetric, it is important to anticipate, as our results will evidence, that the post-buckling modes can be asymmetric, especially for shells with bumpy defects.

The material was modeled as a neo-Hookean solid, with Young's modulus of $E=1.26$ MPa and a Poisson's ratio of $\nu\approx 0.5$ (assuming incompressibility). These material-specific material properties were chosen to align with the previous experimental studies in Refs. [16,22,23,30,32], where they were measured directly from experiments and used to validate the finite-element simulations.

The set of geometric and physical parameters mentioned earlier was chosen to match with Ref. [16] toward enabling a direct comparison with this previous study. However, for the present simulation framework, instead of using the axisymmetry model of Refs. [16,29], we use a three-dimensional description of the structure using shell elements to capture possible asymmetry buckling behavior. This finite-element modeling (FEM) approach has been validated against precision experiments for the specific problem of shell buckling [30,32]. We followed the same FEM methodology to perform simulations with the commercial package ABAQUS/STANDARD; the details are given in Ref. [32]. We employed four-node S4R shell elements with reduced integration points to discretize the shell using sweep meshing, with 300 and 1200 elements in meridional and azimuthal directions, respectively. A mesh convergence study was also conducted to ensure that the results were not influenced by mesh size. A Riks solver [48] was used to capture the progress of the simulation along the arc length of the load–displacement curve. Geometric nonlinearities were considered throughout the study.

In the FEM simulations, each imperfect shell geometry was pressurized until the onset of buckling, at which point the maximum pressure value, p_{max}, was recorded. Then, the knockdown factor was computed using Eq. (2). Throughout the article, for ease of

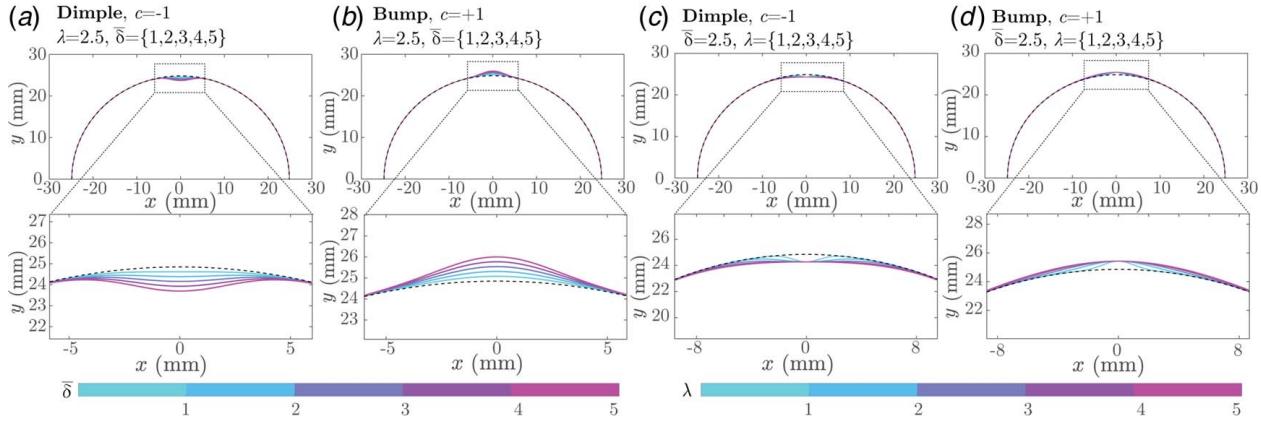

Fig. 2 Representative examples of the initial geometric profiles of the imperfect shells considered. The shells contain defects with (*a*, *b*) $\lambda=2.5$ and $0\le\overline{\delta}\le 5$, and (c, *d*) $\overline{\delta}=2.5$ and $0\le\lambda\le 5$. The defects correspond to dimple, $c=-1$ in (*a*, c) and bump, $c=+1$ in (*b*, *d*). The lower panels show amplified views near the defects. These geometric profiles serve as input to the FEM simulations.

comparison, we will refer to the knockdown factor of the imperfect shell with a dimpled defect as κ_D and κ_B for the bumpy defect. The FEM results for the dimpled shells were first verified against Ref. [16] in the previously explored range of parameters and then expanded to a systematic parameter exploration of dimpled and bumpy defects.

3 Results

Following the methodology introduced earlier, we start our investigation to explore the parameter space of dimpled and bumpy defects. We will characterize and compare the effects of bumps and dimples on the buckling behavior, especially the knockdown factor, of the pressurized imperfect shells.

In Fig. 3, we present surface plots with all the data we obtained from the FEM simulations for the knockdown factor of shells with a dimpled and bumpy imperfection in the whole parameter space ($\bar{\delta}$, λ) specified in Sec. 2: Fig. 3(*a*) for κ_D and Fig. 3(*b*) for κ_B. Color coding is used to quantify the knockdown factor (see the colorbar). Contour lines for constant values of κ_D and κ_B, in intervals of 0.1, are superposed on the surface plots. For the dimpled shells (Fig. 3(*a*)), the minimum value of the knockdown factor, $\kappa_D \approx 0.15$, is found on the upper extremity of the ($\bar{\delta}$, λ) parameter space. This means that a shell with the deepest and widest defect has the lowest knockdown factor, a fact that is well established in the literature. By contrast, for bumpy shells (Fig. 3(*b*)), in the explored range, the minimum knockdown factor ($\kappa_B \approx 0.37$) occurs for the defects with the largest amplitude but intermediate width ($2 \lesssim \lambda \lesssim 3$). Overall, the values of κ_B are consistently larger than those of κ_D; the geometry of dimples plays a more significant role in reducing the knockdown factor of an imperfect shell compared to bumps. These features highlight the first and major qualitative differences between the two cases.

Next, we elaborate on the data presented in Fig. 3 to more comprehensively describe the impact of the various parameters of the defect geometric on the knockdown factor, κ_D for dimples and κ_B for bumps. For this purpose, we first characterize the dependence of the knockdown factor on the defect amplitude and then on the normalized defect width, for both cases.

In Fig. 4, we present κ_D and κ_B as functions of $\bar{\delta}$, each curve corresponding to a different value of λ (see colorbar and marker symbols). The data for shells with dimpled imperfections are shown in Fig. 4(*a*) and those with bumpy imperfections in Fig. 4(*b*).

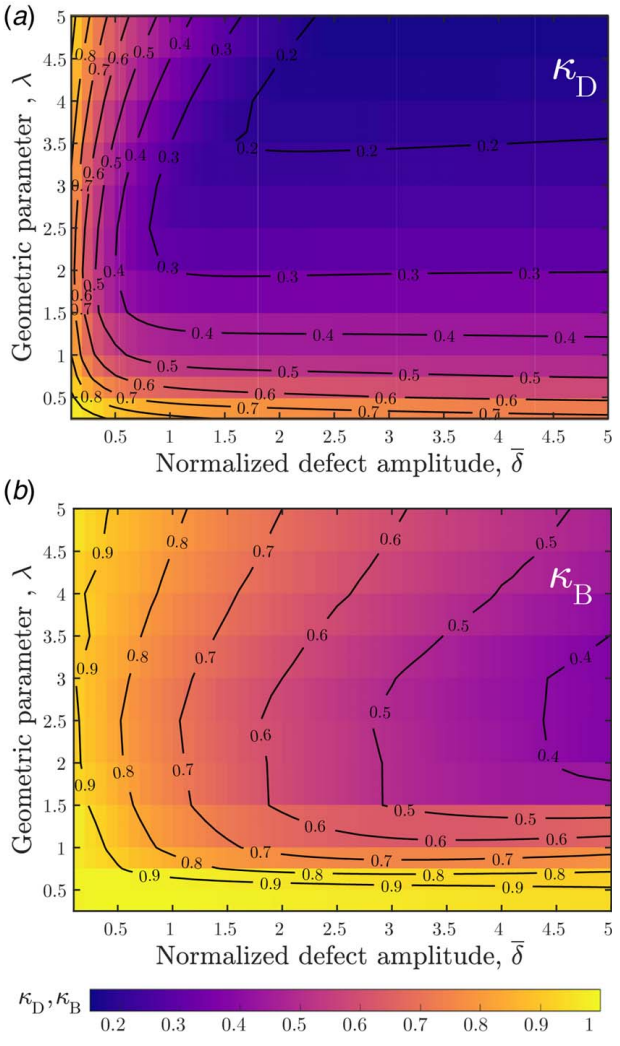

Fig. 3 Surface plots of the knockdown factor of shells containing (*a*) a dimpled imperfection, κ_D, and (*b*) a bumpy imperfection, κ_B, for different values of the dimensionless geometric parameter (width), $0.25 \le \lambda \le 5$, and normalized defect amplitude, $0.1 \le \bar{\delta} \le 5$. Counter lines are superposed for the corresponding values of κ_D and κ_B, in steps of 0.1. Panels (*a*) and (*b*) share the same scale for κ_D and κ_B.

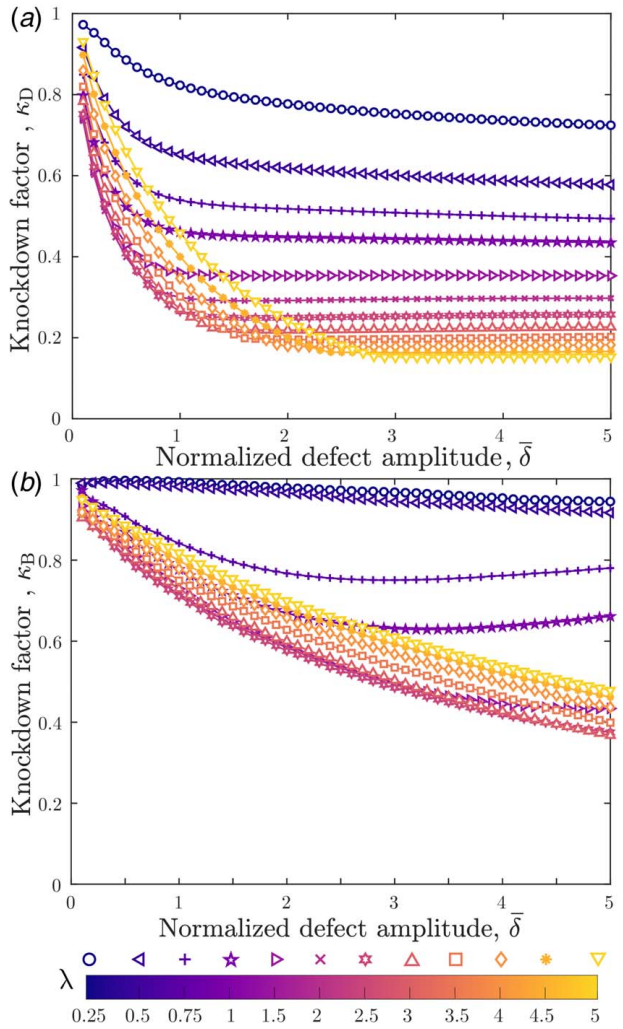

Fig. 4 Knockdown factor, κ, as a function of the normalized defect amplitude, $\bar{\delta}$, for imperfect shells with defects in a range of $\lambda \in [0.25,5]$ (see colorbar and marker symbols): (*a*) Knockdown factor, $\kappa_D(\bar{\delta})$, for a shell with a dimpled imperfection; i.e., $c = -1$ in Eq. (3) and (*b*) Knockdown factor, $\kappa_B(\bar{\delta})$, for a shell with a bumpy imperfection; i.e., $c = +1$ in Eq. (3).

Note that the $\kappa_D(\overline{\delta})$ data in Fig. 4(*a*) are a recomputation of what is already presented in Ref. [16], while the range of geometric parameters for $\lambda < 1$ and $\overline{\delta} > 3$ is further expanded herein. Still, for verification purposes, we selected a specific set of parameters ($\lambda(0 < \overline{\delta} \leq 3) = \{1.5,\ 5\}$) and confirmed identical results to those in Ref. [16]. We recall that in this previously studied case of dimpled imperfections, κ_D decreases monotonically with $\overline{\delta}$ and eventually reaches a plateau. Both the plateau level and its onset depend on λ, as characterized previously in Ref. [29]. The plateau is less pronounced when $\lambda < 1$ (regime not explored previously). For example, in the extreme case of $\lambda = 0.25$ (the narrowest defects), no plateau is reached; after an initially fast decay, the knockdown factor continues to decrease as the amplitude increases all the way to high-amplitude defects of $\overline{\delta} = 5$. We emphasize that there is little novelty in these results for dimpled shells, which were already presented in Ref. [16] and are presented here for completeness to enable a direct comparison with the case of bumpy imperfections discussed next.

Imperfect shells with bumpy defects exhibit a $\kappa_B(\overline{\delta})$ behavior (Fig. 4(*b*)) that is qualitatively different from the dimpled case discussed earlier (Fig. 4(*a*)). The main feature is that the values of κ_B tend to be higher overall than κ_D, with smoother decays as a function of $\overline{\delta}$, and nonmonotonic behavior in some of the curves. Moreover, the κ_B curves do not exhibit the prominent plateaux observed in κ_D. Three regimes are observed. First, for shells with relatively narrow defects, $\lambda = \{0.25,\ 0.5\}$, κ_B remains close to unity across the entire range of $\overline{\delta}$; these shells are nearly insensitive to imperfections. Second, for shells with intermediate-width defects, $\lambda = \{0.75,\ 1\}$, the $\kappa_D(\overline{\delta})$ curves are nonmonotonic; κ_B decreases for $0.1 \leq \delta \lesssim 3$ and then increases beyond $\overline{\delta} \approx 3$. Third, for $\lambda \geq 1.5$, $\kappa_B(\overline{\delta})$ decreases again monotonically.

In Fig. 5, to characterize the knockdown factor behavior with respect to the defect width, we present κ_D for dimpled shells (Fig. 5(*a*)) and κ_B for bumpy shells (Fig. 5(*b*)), as functions of λ. The results are qualitatively the same as shown in Fig. 4. In the case of dimpled shells (Fig. 5(*a*)), for small defect amplitudes, $\overline{\delta} \leq 3$, the $\kappa_D(\lambda)$ curves are nonmonotonic. First, $\kappa_D(\lambda)$ decreases until a threshold defect amplitude and then increases. However, for larger defect amplitudes, $\overline{\delta} \geq 3$, κ_D decreases monotonically. We highlight the fact that the threshold defect amplitude, $\overline{\delta} \approx 3$, corresponds to the largest dimple amplitude before the onset of any of the plateaux for the whole range of λ considered. Past $\overline{\delta} \approx 3$, the $\kappa_D(\lambda)$ curves are monotonic due to the insensitivity of shells to defect amplitude in this regime, for all λ values explored (compared with Fig. 4(*a*)).

Turning to bumpy defects, in Fig. 5(*b*), we plot κ_B versus λ, noting that the behavior is different than their dimpled counterpart (Fig. 5(*a*)). We find that $\kappa_B(\lambda)$ is always non-monotonic, decreasing up to $\lambda \lesssim 2.5$, and then increasing for $\lambda \gtrsim 2.5$. By contrast, for the dimpled shells (Fig. 5(*a*)), $\kappa_D(\lambda)$ was only nonmonotonic when $\overline{\delta} \leq 3$. This distinguishing feature between bumpy and dimpled shells can be attributed to the fact that, in the dimple case, the plateau region is insensitive to defect amplitude, when $\overline{\delta} \geq 3$ for all values of λ; this behavior does not exist in bumpy shells given the absence of any plateauing.

Representative snapshots of post-buckling configurations obtained in the FEM simulations are shown in Fig. 6. The top (x-y) view of the shells is presented in the top row and the isometric (x-y-z) view is in the lower row. We refer to the post-buckling configuration as the first stable mode captured along the pressure–volume path [16] immediately after the onset of buckling. By the way of example, we consider imperfect shells containing a dimpled defect with $\lambda = 2.5$ and $\overline{\delta} = 1.8$ in Fig. 6(*a*) and bumpy defects with $\lambda = 2.5$ and $\overline{\delta} = \{0.3,\ 1.3,\ 2.9,\ 4.4\}$ in Figs. 6(*b*)–6(*e*). The axisymmetric post-buckling configuration in Fig. 6(*a*) is representative of all the dimpled imperfect shells within the explored range of parameters: the buckling initiates at the defect location and expands axisymmetrically outward. The post-buckling configurations are qualitatively distinct for shells with bumpy defects and depend on the value of $\overline{\delta}$; see Figs. 6(*b*)–6(*e*). For

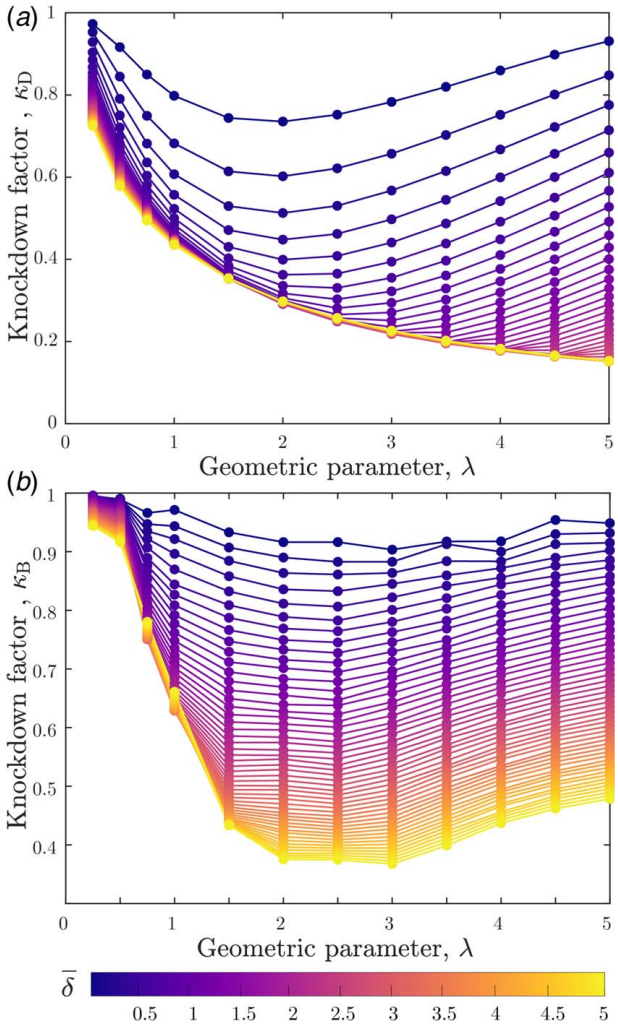

Fig. 5 Knockdown factor, κ, as a function of the normalized defect width, λ, for imperfect shells with defect amplitudes in a range of $\overline{\delta} \in [0.1, 5]$: (*a*) Knockdown factor, $\kappa_D(\lambda)$, for a shell with a dimpled imperfection; i.e., $c = -1$ in Eq. (3) and (*b*) Knockdown factor, $\kappa_B(\lambda)$, for a shell with a bumpy imperfection; i.e., $c = +1$ in Eq. (3).

small defect amplitudes (e.g., $\overline{\delta} = 0.3$, Fig. 6(*b*)), the shell buckles with a periodic deformation mode (akin to wrinkling) near the clamped equator, far from the bumpy defect located at the north pole. It is possible that these results for small-imperfection shells are dominated by imperfections induced by the clamping conditions or by numerical imperfections (artifacts) caused by the meshing. However, in the experimental observations of Ref. [32], we did find that the buckling location is close to the boundary for small bumpy defects, which would tend to suggest that the periodic deformation mode is not an artifact. For higher values of $\overline{\delta}$, the loci of buckling occur near the bumpy defect but nonaxisymmetrically to its side. For example, these post-buckling configurations are lobed with three, two, or one inverted-cap region for $\overline{\delta} = 1.3$, 2.9, and 4.4 , respectively. A detailed analysis of these post-buckling configurations for bumpy shells is beyond the scope of the present study.

Finally, for an even more direct comparison between the dimpled and bumpy cases, in Fig. 7, we convey an alternative representation of the same data reported earlier by plotting κ_D as a function of κ_B. Each data point corresponds to the same pair of ($\overline{\delta}$, λ) parameters for bumps and dimples. Different marker symbols and colors define various values of λ, while the marker size indicates the variation of $\overline{\delta}$. Beyond the specific quantitative observations uncovered

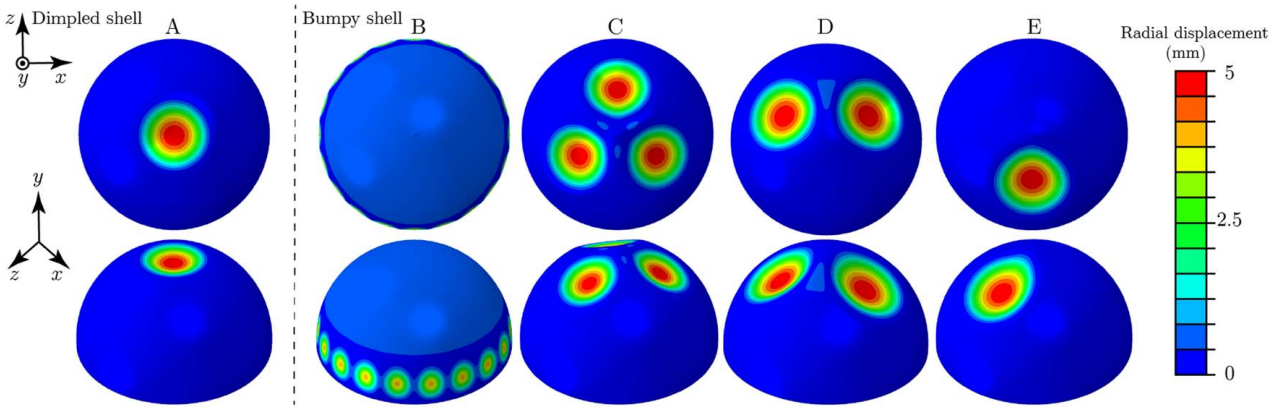

Fig. 6 Representative post-buckling configurations: (*a*) A dimpled post-buckling configuration is representative of all shells containing a dimpled defect (even if the exact values of the radial displacement may differ) and (*b–e*) post-buckling configurations of shells containing a bumpy defect, for the selected cases of $\lambda = 2.5$ and $\overline{\delta} = \{0.3, 1.3, 2.9, 4.4\}$, respectively.

from the data in Figs. 4 and 5, this representation highlights that bumpy shells consistently have a higher buckling strength than dimpled shells, with all of the data lying above the $\kappa_B = \kappa_D$ line (dashed line in Fig. 7). Three different regimes of behavior are observed, similar to Fig. 4(*b*). First, for $\lambda = \{0.25, 0.5\}$, both κ_B and κ_D decrease with the increasing defect amplitude, but the reduction in κ_D is more pronounced than κ_B ought to the lower sensitivity of bumps to defect amplitude in this regime. Second, for $\lambda = \{0.75, 1\}$, we observe a nonmonotonic behavior; with increasing $\overline{\delta}$, first, both κ_D and κ_B decrease until a specific value of $\overline{\delta}$ after which, κ_B increases, while κ_D continues to decreases. Two distinct regions are obvious in the third and last regime for $\lambda \geq 1.5$. Initially, decreasing κ_D follows a decrease in κ_B until the defect amplitude of the plateau onset [29]. After this onset, κ_B continues to decrease, while κ_D remains approximately unchanged (plateau region of insensitivity to defect amplitude).

4 Discussion

In this section, we provide a discussion that seeks to address, even if speculatively, the following emerging questions: Why are bumps stronger than dimples? Why do bumps show different buckling modes of deformation compared to dimples?

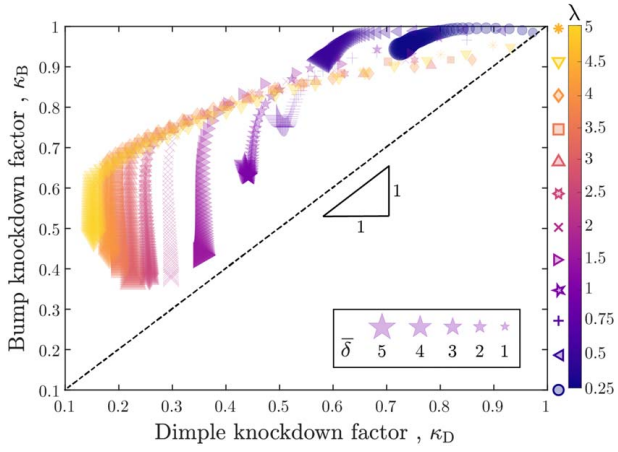

Fig. 7 Knockdown factor of bumpy shells, κ_B, versus that of dimpled shells, κ_D, for a range of dimensionless defect geometric parameters, $0.25 \leq \lambda \leq 5$, and defect amplitudes, $0.1 \leq \overline{\delta} \leq 5$. The values of λ are coded by the shade in the adjacent bar, and the values of $\overline{\delta}$ are represented by the size of the symbol (see legend). The dashed line represents $\kappa_B = \kappa_D$.

The dimpled and bumpy shells are only distinguishable by their defect region located at the pole, with $c = \pm 1$ in Eq. (3). We focus on the difference in the geometry of their undeformed (initial) configuration, as measured by the mean and Gaussian curvatures profiles defined, respectively, as follows:

$$\mathcal{K}_H(\beta) = \frac{1}{2}(k_1 + k_2)$$
$$\mathcal{K}_G(\beta) = k_1 k_2 \tag{5}$$

where k_1 and k_2 are the two principal (local) curvatures of the shell surface. We have numerically computed $\mathcal{K}_H$ and $\mathcal{K}_G$ with the function `surfature` [49] in *MATLAB*, taking the point-cloud data representation of the undeformed surface as input for the FEM simulations. We will add the subscripts D and B to denote the corresponding quantities for dimples and bumps, respectively, i.e., ($\mathcal{K}_{HD}$, $\mathcal{K}_{HB}$) and ($\mathcal{K}_{GD}$, $\mathcal{K}_{GB}$).

In Fig. 8, we plot the mean curvature, $\mathcal{K}_H$, in (*a*) and (*b*), and the Gaussian curvature, $\mathcal{K}_G$, in (*c*) and (*d*), as functions of the polar angle, β. The angular width of the defect, $\beta_\circ$, defined in Eq. (3), is represented by the vertical dashed lines. We restrict our results to the representative case with $\lambda = 2.5$ (where the knockdown factor of bumpy shells is lowest) while varying the defect amplitudes $\overline{\delta} = \{1, 2, 3, 4, 5\}$ (see color bar). Figures 8(*a*) and 8(*c*) correspond to the dimpled shells, and Figs. 8(*b*) and 8(*d*) correspond to the bumpy shells. Qualitatively similar behavior to what we describe next is found for other values of λ, but a detailed quantitative analysis is beyond the scope of the present work and unnecessary to the qualitative interpretation that we will provide.

Hereon, we shall refer to the $\beta < \beta_\circ$ region as the *core* of the defect and to the neighboring region right past the defect, $\beta \gtrsim \beta_\circ$, as the *rim* of the defect. The mean-curvature curves for dimpled shells, $\mathcal{K}_{HD}(\beta)$ (Fig. 8(*a*)), exhibit a maximum located at the defect rim. Within the defect core, by construction, the dimples have a minimum mean curvature that is typically negative and always lower than that of the nominal spherical shell. By contrast, for the bumpy shells, all the $\mathcal{K}_{HB}(\beta)$ curves have a minimum located at the defect rim (Fig. 8(*b*)). At the defect core, the bumps have positive mean curvature, always greater than that far away in the shell.

Rewording the aforementioned observations, it is important to highlight that the minimum of $\mathcal{K}_H$ occurs at the core for dimples and at the rim for bumps. Conversely, the maximum of $\mathcal{K}_H$ occurs at the rim for dimples and at the core for bumps. As evidenced in Fig. 6 and studied extensively in the literature, a depressurized imperfect spherical shell exhibits a buckling mode with one

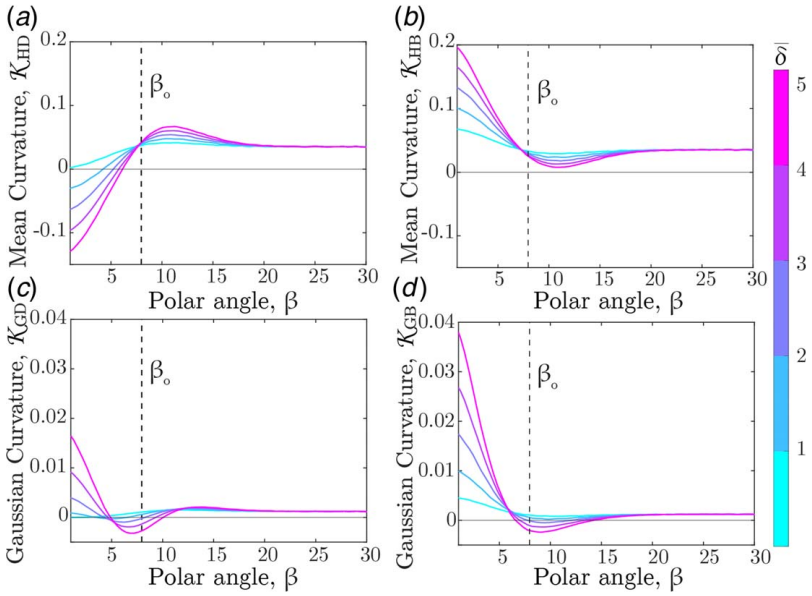

Fig. 8 Curvature profiles of the initial geometry of the imperfect shell as a function of the polar angle, β. Representative cases are chosen with the dimensionless geometric parameter of $\lambda = 2.5$, and amplitudes in a range of $\bar{\delta} \in [1, 5]$: (*a*) Mean curvature, $\mathcal{K}_{HD}$, and (c) Gauss curvature, $\mathcal{K}_{GD}$, for a shell with a dimpled imperfection; i.e., $c = -1$ in Eq. (3). (*b*) Mean curvature, $\mathcal{K}_{HB}$, and (*d*) Gauss curvature, $\mathcal{K}_{GB}$, for a shell with a bumpy imperfection; i.e., $c = +1$ in Eq. (3). The vertical dashed line indicates $\beta_\circ$, the defect opening angle corresponding to $\lambda = 2.5$.

(or more) inward-inverted cap, whose mean curvature has the opposite sign of the nominal sphere. It is reasonable to envision that regions of mean curvature lower (or higher) than that of the nominal sphere will serve as weak (or strong) spots, respectively. This reasoning, even if speculative, is compatible with the results shown in Fig. 6. For dimples (Fig. 6(*a*)), the post-buckling configuration does indeed occur at the defect core, where $\mathcal{K}_H$ is minimum. For bumps (Figs. 6(*b*)–6(*d*)), the buckling appears to nucleate at the defect rim, where $\mathcal{K}_H$ is minimum, and repelled by the defect core, which appears to have a stiffening effect. Moreover, the fact that $\mathcal{K}_H$ is always positive in the considered range of $\bar{\delta}$ may be the source of why the knockdown factor of bumpy shells is consistently higher than that of dimpled shells.

Regarding the Gaussian curvature data presented in Figs. 8(*c*) and 8(*d*), the results are, as far as we can tell, less insightful. We observe that at the defect core, $\mathcal{K}_G$ is higher for the bumpy than the dimpled shells, which may further contribute to the lower buckling strength of the latter (for the same magnitude of geometric parameters). Otherwise, both cases display Gaussian curvature profiles that are qualitatively similar. All $\mathcal{K}_G$ curves are nonmonotonic with a minimum near the defect rim, occurring before (or after) $\beta_\circ$ for dimples (or bumps), respectively. In both cases, this minimum can be negative for defects with larger amplitudes ($\bar{\delta} \gtrsim 1$ for the dimples and $\bar{\delta} \gtrsim 3$ for the bumps) but always positive otherwise. Outside of this region of the minimum neighboring the rim, $\mathcal{K}_G > 0$ in both cases. Overall, we do not see any salient qualitative differences in the $\mathcal{K}_G$ between the dimpled and bumpy cases that correlate to the $\kappa_D > \kappa_B$ reported in Fig. 7 and earlier plots.

There are similarities between the geometry of the bumpy shells we considered and the classical literature for the Cohn-Vossen's shape [50]. Shells with nonconstant and sign-changing Gaussian curvature can be a source of an exceptional bending mode on a surface of revolution [51]. It is possible that this behavior can be related to the different buckling modes we observed in our bumpy shells, although we have no formal ground other than reasoning by analogy to support this statement. Future theoretical work will be necessary to further rationalize the present findings, which point to the importance of the detailed curvature profiles of doubly curved imperfect shells, with a special spotlight on their mean curvature.

5 Conclusion

We used an existing finite-element simulations approach, which was validated previously against experiments, to study the buckling strength of imperfect shells containing either a dimpled or a bumpy imperfection. Although dimpled shells have been studied previously in much detail, bumpy shells have remained largely unexplored. We considered defects with a standard Gaussian profile (compared with Eq. (3)), enabling direct and detailed comparisons across the dimpled ($c = -1$) and bumpy ($c = +1$) cases. Our results evidence that the role of bumps in reducing the buckling strength of the spherical shell is less dramatic than for dimples, at least within the ranges of parameters we explored. The knockdown factor sensitivity to the detailed defect geometry is also less prominent in bumps. Overall, the knockdown factor of a bumpy shell is always greater than that of a dimpled one, $\kappa_B > \kappa_D$, for the same magnitude of geometric parameters. In both cases, the knockdown factor is not always reduced when the defect is widened.

We attempted to discuss the differences in knockdown factor between dimpled and bumpy shells under the light of their mean and Gaussian curvature profiles. Our interpretation suggests that regions of the imperfect shell with minimal mean curvature serve as weak points for the onset of buckling. These minima occur at the defect core for dimpled shells and at the defect rim for bumpy shells. For the latter, the core appears to have a stiffening effect, which repels the post-buckling inverted caps making the buckling mode asymmetric and potentially multi-lobed.

We acknowledge that our investigation was mostly descriptive and observational. In the absence of the formal theoretical framework, it is difficult to devise a predictive rationale for these observations. Still, we hope that our thorough comparative study will be valuable in the ongoing revival of shell-buckling studies. A

systematic theoretical investigation will be a much-needed next step in rationalizing the current findings. In addition, it would be interesting to consider other imperfection geometries and establish direct relations between the mean/Gaussian curvature profiles and the resulting critical buckling conditions. Shell buckling is a highly nonlinear and nontrivial phenomenon, and we believe that specific case studies like ours are essential to gaining insight and motivating modeling directions.

From a practical viewpoint, our research is aligned with efforts currently underway by NASA and others interested in large-scale shell structures [52–54]. These efforts aim to replace the purely empirical knockdown factors guidelines in design codes of aerospace structures with mechanics-based predictive methods that take manufacturing-based data on the imperfection distributions as input. Our results demonstrate that different types of defects, even if characterized by similar geometric parameters, can yield quantitatively and qualitatively different reductions of buckling strength. For example, the design of shells containing only bumpy defects can be tackled less conservatively than dimpled shells.

Acknowledgment

A.A. thanks the Federal Commission for Scholarships for Foreign Students (FCS) support through a Swiss Government Excellence Scholarship (Grant No. 2019.0619). We are also grateful to John Hutchinson for his encouragement. During the initial stages of our investigation, he shared with us earlier preliminary findings of his suggesting a distinct buckling behavior between dimpled and bumpy shells. These nurturing interactions drove our motivation to tackle the thorough comparison in the present study.

Conflict of Interest

There are no conflicts of interest.

Data Availability Statement

The datasets generated and supporting the findings of this article are obtainable from the corresponding author upon reasonable request.

References

[1] Niordson, F., 1985, *Shell Theory* (North-Holland Series in Applied Mathematics and Mechanics), Elsevier Science, Amsterdam.
[2] Koiter, W. T., 1969, "The Nonlinear Buckling Behavior of a Complete Spherical Shell Under Uniform External Pressure, Parts I, II, III & IV," Proc. Kon. Ned. Ak. Wet., **B72**(1), pp. 40–123.
[3] Von Karman, T., and Tsien, H.-S., 1939, "The Buckling of Spherical Shells by External Pressure," J. Aeronaut. Sci., **7**(2), pp. 43–50.
[4] Von Karman, T., Dunn, L. G., and Tsien, H.-S., 1940, "The Influence of Curvature on the Buckling Characteristics of Structures," J. Aeronaut. Sci., **7**(7), pp. 276–289.
[5] Koiter, W. T., 1945, "Over de stabiliteit van het elastisch evenwicht," Ph.D. thesis, Delft University of Technology, Delft, The Netherlands.
[6] Hutchinson, J., and Koiter, W., 1970, "Postbuckling Theory," ASME Appl. Mech. Rev., **23**(12), pp. 1353–1366.
[7] Elishakoff, I., 2014, *Resolution of the Twentieth Century Conundrum in Elastic Stability*, World Scientific Publishing, Singapore.
[8] Samuelson, L. A., and Eggwertz, S., 2003, *Shell Stability Handbook*, Elsevier Applied Science, London.
[9] Zoelly, R., 1915, "Ueber Ein Knickungsproblem An Der Kugelschale," Ph.D. thesis, ETH Zürich, Zürich, Switzerland.
[10] Seaman, L., 1962, "The Nature of Buckling in Thin Spherical Shells," Ph.D. thesis, Massachusetts Institute of Technology, Cambridge, MA.
[11] Kaplan, A., and Fung, Y., 1954, "A Nonlinear Theory of Bending and Buckling of Thin Elastic Shallow Spherical Shells," National Advisory Committee for Aeronautics, WA, DC, Technical Note 3212.
[12] Tsien, H.-S., 1942, "A Theory for the Buckling of Thin Shells," J. Aeronaut. Sci., **9**(10), pp. 373–384.
[13] Krenzke, M., and Kiernan, T., 1963, "Elastic Stability of Near-Perfect Shallow Spherical Shells," AIAA J., **1**(12), pp. 2855–2857.
[14] Babcock, C., 1983, "Shell Stability," ASME J. Appl. Mech., **50**(4b), pp. 935–940.
[15] Carlson, R. L., Sendelbeck, R. L., and Hoff, N. J., 1967, "Experimental Studies of the Buckling of Complete Spherical Shells," Exp. Mech., **7**(7), pp. 281–288.
[16] Lee, A., López Jiménez, F., Marthelot, J., Hutchinson, J. W., and Reis, P. M., 2016, "The Geometric Role of Precisely Engineered Imperfections on the Critical Buckling Load of Spherical Elastic Shells," ASME J. Appl. Mech., **83**(11), p. 111005.
[17] Bijlaard, P., and Gallagher, R., 1960, "Elastic Instability of a Cylindrical Shell Under Arbitrary Circumferential Variation of Axial Stress," J. Aerosp. Sci., **27**(11), pp. 854–858.
[18] Kobayashi, S., 1968, "The Influence of the Boundary Conditions on the Buckling Load of Cylindrical Shells Under Axial Compression," J. Jpn. Soc. Aeronaut. Eng., **16**(170), pp. 74–82.
[19] Almroth, B. O., 1966, "Influence of Edge Conditions on the Stability of Axially Compressed Cylindrical Shells," AIAA J., **4**(1), pp. 134–140.
[20] Budiansky, B., and Hutchinson, J. W., 1972, "Buckling of Circular Cylindrical Shells Under Axial Compression,"*Contributions to the Theory of Aircraft Structures*, Delft University Press, Nijgh-Wolters-Noordhoff University Publishers, Rotterdam, The Netherlands, pp. 239–260.
[21] Lee, A., Brun, P.-T., Marthelot, J., Balestra, G., Gallaire, F., and Reis, P. M., 2016, "Fabrication of Slender Elastic Shells by the Coating of Curved Surfaces," Nat. Commun., **7**, p. 11155.
[22] Marthelot, J., López Jiménez, F., Lee, A., Hutchinson, J. W., and Reis, P. M., 2017, "Buckling of a Pressurized Hemispherical Shell Subjected to a Probing Force," ASME J. Appl. Mech., **84**(12), p. 121005.
[23] Yan, D., Pezzulla, M., and Reis, P. M., 2020, "Buckling of Pressurized Spherical Shells Containing a Through-Thickness Defect," J. Mech. Phys. Solids, **138**(26), p. 103923.
[24] Lee, A., Yan, D., Pezzulla, M., Holmes, D. P., and Reis, P. M., 2019, "Evolution of Critical Buckling Conditions in Imperfect Bilayer Shells Through Residual Swelling," Soft. Matter., **15**(30), pp. 6134–6144.
[25] Virot, E., Kreilos, T., Schneider, T. M., and Rubinstein, S. M., 2017, "Stability Landscape of Shell Buckling," Phys. Rev. Lett., **119**(22), p. 224101.
[26] Gerasimidis, S., Virot, E., Hutchinson, J. W., and Rubinstein, S. M., 2018, "On Establishing Buckling Knockdowns for Imperfection-Sensitive Shell Structures," ASME J. Appl. Mech., **85**(9), p. 091010.
[27] Fan, H., 2019, "Critical Buckling Load Prediction of Axially Compressed Cylindrical Shell Based on Non-Destructive Probing Method," Thin-Walled Struct., **139**(33), pp. 91–104.
[28] Lazarus, A., Florijn, H. C. B., and Reis, P. M., 2012, "Geometry-Induced Rigidity in Nonspherical Pressurized Elastic Shells," Phys. Rev. Lett., **109**, p. 144301.
[29] López Jiménez, F., Marthelot, J., Lee, A., Hutchinson, J. W., and Reis, P. M., 2017, "Technical Brief: Knockdown Factor for the Buckling of Spherical Shells Containing Large-Amplitude Geometric Defects," ASME J. Appl. Mech., **84**(3), p. 034501.
[30] Abbasi, A., Yan, D., and Reis, P. M., 2021, "Probing the Buckling of Pressurized Spherical Shells," J. Mech. Phys. Solids, **155**(21), p. 104545.
[31] Pezzulla, M., and Reis, P. M., 2019, "A Weak Form Implementation of Nonlinear Axisymmetric Shell Equations With Examples," ASME J. Appl. Mech., **86**(12), p. 124502.
[32] Derveni, F., Gueissaz, W., Yan, D., and Reis, P. M., 2023, "Probabilistic Buckling of Imperfect Hemispherical Shells Containing a Distribution of Defects," 381(2244). 8
[33] Hutchinson, J. W., and Thompson, J. M. T., 2018, "Imperfections and Energy Barriers in Shell Buckling," Int. J. Solids Struct., **148–149**, pp. 157–168.
[34] Hutchinson, J. W., and Thompson, J. M. T., 2017, "Nonlinear Buckling Interaction for Spherical Shells Subject to Pressure and Probing Forces," ASME J. Appl. Mech., **84**(6), p. 061001.
[35] 2017, "Nonlinear Buckling Behaviour of Spherical Shells: Barriers and Symmetry-Breaking Dimples," P. Roy. Soc. A-Math. Phy., **375**(2093), p. 20160154.
[36] Hutchinson, J. W., and Thompson, J. M. T., 2018, "Imperfections and Energy Barriers in Shell Buckling," Int. J. Solids Struct., **148**(15), pp. 157–168.
[37] Homewood, R. H., Brine, A. C., and Johnson, A. E., 1961, "Experimental Investigation of the Buckling Instability of Monocoque Shells," Exp. Mech., **1**(3), pp. 88–96.
[38] Von Karman, T., and Tsien, H.-S., 1941, "The Buckling of Thin Cylindrical Shells Under Axial Compression," J. Aeronaut. Sci., **8**(8), pp. 303–312.
[39] Groh, R., and Pirrera, A., 2017, *Exploring Islands of Stability in the Design Space of Cylindrical Shell Structures*, CRC Press, Boca Raton, FL.
[40] Groh, R. M., and Pirrera, A., 2019, "Spatial Chaos as a Governing Factor for Imperfection Sensitivity in Shell Buckling," Phys. Rev. E, **100**(3), p. 032205.
[41] Hutchinson, J. W., 2016, "Buckling of Spherical Shells Revisited," P. Roy. Soc. A-Math. Phys., **472**(2195), p. 20160577.
[42] Thompson, J. M. T., and Sieber, J., 2016, "Shock-Sensitivity in Shell-Like Structures: With Simulations of Spherical Shell Buckling," Int. J. Bif. Chaos, **26**(2), p. 1630003.
[43] Thompson, J. M. T., Hutchinson, J. W., and Sieber, J., 2017, "Probing Shells Against Buckling: a Nondestructive Technique for Laboratory Testing," Int. J. Bif. Chaos, **27**(14), p. 1730048.
[44] Hutchinson, J. W., Muggeridge, D. B., and Tennyson, R. C., 1971, "Effect of a Local Axisymmetric Imperfection on the Buckling Behaviorof a Circular Cylindrical Shell Under Axial Compression," AIAA J., **9**(1), pp. 48–52.

[45] Paulose, J., and Nelson, D. R., 2013, "Buckling Pathways in Spherical Shells With Soft Spots," Soft. Matter., **9**(34), pp. 8227–8245.
[46] Gerasimidis, S., and Hutchinson, J., 2021, "Dent Imperfections in Shell Buckling: The Role of Geometry, Residual Stress, and Plasticity," ASME J. Appl. Mech., **88**(3), p. 031007.
[47] Koga, T., and Hoff, N. J., 1969, "The Axisymmetric Buckling of Initially Imperfect Complete Spherical Shells," Int. J. Solids Struct., **5**(7), pp. 679–697.
[48] Riks, E., 1979, "An Incremental Approach to the Solution of Snapping and Buckling Problems," Int. J. Solids Struct., **15**(7), pp. 529–551.
[49] Claxton, D., 2023, "Surface Curvature, Matlab Central File Exchange," https://www.mathworks.com/matlabcentral/fileexchange/11168-surface-curvature.
[50] Cohn-Vossen, S., 1929, "Unstarre Geschlossene Flachen," Math. Ann., **102**(1), p. 10.
[51] Audoly, B., and Pomeau, Y., 2010, *Elasticity and Geometry: From Hair Curls to the Non-linear Response of Shells*, Oxford University Press, Oxford, UK.
[52] Hilburger, M. W., Nemeth, M. P., and Starnes Jr, J. H., 2006, "Shell Buckling Design Criteria Based on Manufacturing Imperfection Signatures," AIAA J., **44**(3), pp. 654–663.
[53] Hilburger, M., 2012, "Developing the Next Generation Shell Buckling Design Factors and Technologies," 53rd AIAA/ASME/ASCE/AHS/ASC Structures, Structural Dynamics and Materials Conference 20th AIAA/ASME/AHS Adaptive Structures Conference 14th AIAA, Honolulu, HI, Apr. 23–26, p. 1686.
[54] Castro, S. G., Zimmermann, R., Arbelo, M. A., Khakimova, R., Hilburger, M. W., and Degenhardt, R., 2014, "Geometric Imperfections and Lower-Bound Methods Used to Calculate Knock-Down Factors for Axially Compressed Composite Cylindrical Shells," Thin-Walled Struct., **74**(26), pp. 118–132.